https://doi.org/10.5194/egusphere-2025-5917
Preprint. Discussion started: 8 December 2025

Subsurface dissolution reduces the efficiency of mineral-based ocean alkalinity enhancement

Friedrich A. Burger[1,2], Urs Hofmann Elizondo[1,2], Hendrik Grosselindemann[1,2], and Thomas L. Frölicher[1,2]

[1]Climate and Environmental Physics, Physics Institute, University of Bern, Bern, Switzerland.
[2]Oeschger Centre for Climate Change Research, University of Bern, Bern, Switzerland.

Correspondence: Friedrich Burger (friedrich.burger@unibe.ch)

Abstract. Carbon dioxide removal (CDR) from the atmosphere will likely be required to offset hard-to-abate emissions and limit global warming to well below 2°C, in line with the Paris Agreement. Among proposed CDR strategies, ocean alkalinity enhancement (OAE) is increasingly discussed because it offers high carbon sequestration potential, long storage timescales, and potentially mitigates ocean acidification. OAE is often envisioned through the dissolution of alkaline mineral powders, such as the silicate mineral forsterite, the most abundant form of olivine. Fine-grained powders dissolve near the surface, where the added alkalinity can efficiently enhance oceanic carbon uptake, whereas coarser grains sink and dissolve at depth. Most modeling studies assume complete surface dissolution, leaving the impact of subsurface dissolution on ocean carbon uptake poorly understood. Here, we develop idealized vertical mineral dissolution profiles that vary with environmental conditions and grain size. These profiles are implemented in a comprehensive Earth system model to assess the capture efficiency of OAE, defined as the additional carbon taken up by the ocean per alkalinity added. We find that the efficiency is very sensitive to grain size and may decrease by more than 75% when grain size doubles, as larger grains release the alkalinity at deeper depth. Efficiency further decreases when particles are not uniformly sized but follow a particle size distribution with the same mean particle volume. In addition, efficiency is time-dependent: it is lower in the first decades of OAE and increases as alkalinity previously released in the ocean interior eventually resurfaces, often far from deployment sites. For forsterite particles with diameter 3.4 μm, the efficiency is less than one-fourth of that achieved with surface alkalinity addition over the first decade, less than one-third over the first 30 years, and less than half over 175 years. Our results indicate that olivine may be substantially less effective for open-ocean alkalinity enhancement and carbon removal than previously assumed and that the delayed, spatially dispersed carbon uptake presents major challenges for monitoring, reporting and verification.

1 Introduction

Carbon dioxide removal (CDR) is widely considered necessary for achieving net-zero CO_2 emissions targets and limiting global warming in line with the Paris Agreement (Babiker et al., 2022). Among various CDR approaches, marine-based methods have gained growing scientific and policy interest. In particular, ocean alkalinity enhancement (OAE) has emerged as a

https://doi.org/10.5194/egusphere-2025-5917
Preprint. Discussion started: 8 December 2025

promising option due to its well-understood carbonate chemistry, high carbon sequestration potential, long storage capacity (Boyd and Vivian, 2019; Canadell et al., 2021), and its potential for ocean acidification mitigation (Doney et al., 2024).

OAE is often thought to be implemented by adding alkaline mineral powders, such as the silicate mineral olivine, to the open ocean surface, where dissolution increases seawater alkalinity and enhances carbon uptake from the atmosphere (Köhler et al., 2010; National Academies of Sciences, Engineering, and Medicine, 2022). Global modeling studies of OAE commonly assume instantaneous and complete alkalinity release at the ocean surface (Keller et al., 2014; Nagwekar et al., 2024; Schwinger et al., 2024; Tyka, 2025; Zhou et al., 2025). However, this assumption holds only if the added minerals dissolve rapidly, which depends strongly on particle size (Boyd and Vivian, 2019; National Academies of Sciences, Engineering, and Medicine, 2022). Coarser particles dissolve slowly and sink quickly, releasing alkalinity at deeper depths rather than near the surface. Alkalinity released in the ocean interior contributes to oceanic carbon uptake only when those waters re-emerge at the surface, a process that can take decades to centuries depending on the regional ocean ventilation timescales. Conversely, grinding minerals to finer sizes increases dissolution rates but increases life-cycle energy demand and associated CO_2 emissions (Foteinis et al., 2023).

A few studies have analyzed the mineral dissolution dynamics, particularly for the silicate mineral olivine, using simplified analytical shrinking core models that idealize mineral particles as smooth spheres (Hangx and Spiers, 2009). These models have been used to estimate dissolution times and carbon uptake in coastal OAE settings (Hangx and Spiers, 2009; Feng et al., 2017) and to approximate alkalinity release within the surface mixed layer of the open ocean (Köhler et al., 2013; Renforth and Kruger, 2013; Yang et al., 2025). In contrast, Fakhraee et al. (2023) employed a complex mineral particle model to simulate alkalinity release in an Earth system model of reduced complexity and coarse spatial resolution. These studies show that dissolution time increases strongly with particle size, highlight regional differences in mixed layer alkalinity release, and identify potential interactions between seeded particles and planktonic communities. Nevertheless, we currently lack knowledge about the impact of particle sinking during dissolution on OAE efficiency, which needs to be assessed with ocean-biogeochemical models or Earth system models.

Here, we analyze the efficiency of mineral-based OAE using a comprehensive, fully coupled Earth system model that explicitly accounts for the interplay between particle sinking and dissolution, represented through a shrinking core model (Hangx and Spiers, 2009). We derive simple analytical vertical alkalinity release profiles and apply them as boundary conditions to the Earth system model. The analysis focuses on the influence of particle size, particle size distribution, and deployment location on alkalinity release and OAE-induced carbon uptake, with a focus on the alkaline silicate mineral olivine, often considered for its relatively high dissolution rate compared to other silicate minerals. Section 2 describes the alkalinity release profiles, the treatment of varying environmental conditions for these profiles, as well as the experimental design for the Earth system model. Section 3 presents the resulting regional variations in the vertical alkalinity release profiles and quantifies the sensitivity of carbon uptake efficiency to particle size, both for uniform particles and a particle size distribution. The results and their limitations are discussed in section 4.

https://doi.org/10.5194/egusphere-2025-5917
Preprint. Discussion started: 8 December 2025

2 Methods

2.1 Alkalinity release profiles

2.1.1 Particle dissolution in the shrinking core model

We consider spherical particles with a dissolution rate that is proportional to the surface area (constant area-normalized dissolution rate r in mol m^{-2} s^{-1}). The decrease in the number of moles of the mineral stored in the particle N_p per time is given by the product of r and the surface area A:

$$\frac{\mathrm{d}N_p}{\mathrm{d}t} = -r \cdot A \tag{1}$$

As a result, the particle radius (R) decreases linearly with time (see also Hangx and Spiers, 2009):

$$\frac{\mathrm{d}R}{\mathrm{d}t} = \underbrace{\frac{\mathrm{d}R}{\mathrm{d}V}}_{=1/A} \cdot \underbrace{\frac{\mathrm{d}V}{\mathrm{d}N_p}}_{=V_{\mathrm{mol}}} \cdot \frac{\mathrm{d}N_p}{\mathrm{d}t} = -r \cdot V_{\mathrm{mol}} \tag{2}$$

with V_{mol} as the molar volume of the mineral (the molar mass of the mineral divided by its density). Such a simple particle dissolution model is referred to as a *shrinking core model*. When this particle is sinking with speed v_{sink} during dissolution, the change in N_p per depth is given by the change per time divided by sinking speed:

$$\frac{\mathrm{d}N_p}{\mathrm{d}z} = \frac{\mathrm{d}N_p}{\mathrm{d}t} \cdot \frac{1}{v_{\mathrm{sink}}} = -\frac{r \cdot A}{v_{\mathrm{sink}}}. \tag{3}$$

The term v_{sink} is the Stokes settling velocity of a sinking spherical particle of radius R,

$$v_{\mathrm{sink}} = \frac{2(\rho_{\mathrm{p}} - \rho_{\mathrm{w}})gR^2}{9\mu}, \tag{4}$$

with the gravitational acceleration g, particle density ρ_{p}, seawater density ρ_{w}, and the dynamic viscosity of seawater μ. Since both v_{sink} and the particle surface area $A = 4\pi R^2$ are proportional to R^2, the dependence of $\mathrm{d}N_p/\mathrm{d}z$ on R cancels out and $\mathrm{d}N_p/\mathrm{d}z$ does not change with particle size. Intuitively speaking, larger particles release more alkalinity per unit time due to their larger surface area, but also sink faster, such that they lose the same number of moles per depth as a smaller particle.

The reference depth z_0 is the depth at which a particle with an initial radius R is completely dissolved. It is given by

$$z_0 = \underbrace{N_p(0)}_{V_R/V_{\mathrm{mol}}} \Big/ \left(-\frac{\mathrm{d}N_p}{\mathrm{d}z}\right) = \frac{(\rho_p - \rho_w)gV_R}{18\pi\mu r V_{\mathrm{mol}}} = \frac{2(\rho_p - \rho_w)gR^3}{27\mu r V_{\mathrm{mol}}}. \tag{5}$$

The reference depth z_0 is much larger for larger particles, since it is proportional to the initial particle volume $V_R = \frac{4}{3}\pi R^3$, and thus proportional to the cube of its initial particle radius.

2.1.2 Alkalinity release profile for a flux of uniform particles

With a flux of incoming mineral particles F_p (number of particles per m^2 s^{-1}), the total alkalinity (A_{T}) release per unit time at depth z (z defined positive and increasing with depth) is the product of the incoming particle flux and the alkalinity release of

https://doi.org/10.5194/egusphere-2025-5917
Preprint. Discussion started: 8 December 2025

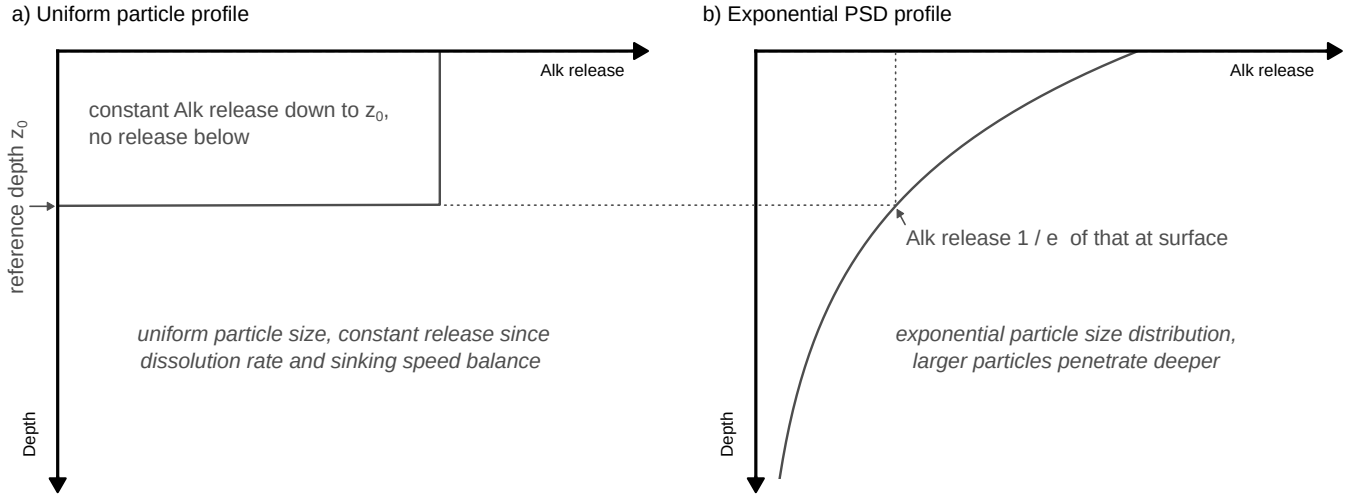

Figure 1. Alkalinity release profiles for a) uniform particles (section 2.1.2) and b) for particles with an exponential particle size distribution (section 2.1.3).

each particle:

$$\frac{\mathrm{d}A_\mathrm{T}}{\mathrm{d}t}(z) = F_p \cdot \left(-\frac{\mathrm{d}N_p}{\mathrm{d}z}\right) \cdot n_{Alk} = \begin{cases} \dfrac{F}{z_0} & \text{for } z \le z_0 \\ 0 & \text{for } z > z_0\,. \end{cases} \tag{6}$$

with alkalinity in units $\mathrm{mol\,m^{-3}}$. The factor n_{Alk} represents the alkalinity release per dissolved mineral molecule ($n_{Alk} = 4$ for olivine). F denotes the flux of alkalinity stored in the mineral particles entering the ocean (in $\mathrm{mol\,m^{-2}s^{-1}}$), related to the particle flux F_p through $F = F_p \cdot N_p(0) \cdot n_{Alk}$. Similarly as before, the factor n_{Alk} here translates from the initial number of moles of the mineral in each particle to the corresponding number of moles of alkalinity. Thus, the alkalinity release per unit time is simply given by the mineral alkalinity flux F applied to the surface divided by the reference depth z_0 for $z \le z_0$ and vanishing for $z > 0$. The alkalinity release profile for uniform particles is depicted in Figure 1a and validated by an explicit numerical simulation of sinking particles in Appendix Figure A1.

2.1.3 Alkalinity release profile for an exponential particle size distribution

Now, we consider the case where the mineral particles are not uniform but follow a certain particle size distribution (PSD). To this end, we assume an exponential PSD for particle volume (or equivalently mass)

$$f(V, V_R) = \frac{1}{V_R} e^{-V/V_R}. \tag{7}$$

The parameter $V_R = \frac{4}{3}\pi R^3$, the particle volume for the reference radius R, is the mean particle volume across the PSD. Hence, the PSD does not change the average particle volume and alkalinity content, but adds a certain dispersion around this average

https://doi.org/10.5194/egusphere-2025-5917
Preprint. Discussion started: 8 December 2025

value. From the exponential distribution, one can calculate the percentiles for particle radius, given by $R_x = \left(\ln \frac{1}{1-x}\right)^{1/3} R$. For example, for $x = 0.8$ one obtains the 80th percentile. The fraction of particle volume or mass above a percentile is given by $(1-x)\left(1+\ln \frac{1}{1-x}\right)$.

This PSD can now be used to derive the corresponding alkalinity release profile. As discussed before, each particle within the exponential PSD releases the same alkalinity per unit depth. However, smaller particles from the PSD vanish with increasing depth, such that the overall alkalinity release at depth originates from the remaining larger particles and leading to a decrease in alkalinity release with depth.

Equation 5 can be used to determine the minimum initial volume (V_{min}) for which a particle is still present at depth z. Realizing that $z/V_{\text{min}} = z_0/V_R$, one obtains

$$V_{\text{min}}(z) = V_R \cdot \frac{z}{z_0}. \tag{8}$$

The alkalinity release per unit time at depth z is the product of the remaining incoming particles at depth z and the alkalinity release of each particle:

$$\frac{\mathrm{d}A_{\text{T}}}{\mathrm{d}t}(z) = \left(F_p \cdot \int_{V_{\text{min}}(z)}^{\infty} f(V, V_R)\mathrm{d}V \right) \cdot \left(-\frac{\mathrm{d}N_p}{\mathrm{d}z} \right) \cdot n_{Alk} = \left(F_p \cdot e^{-V_{\text{min}}(z)/V_R} \right) \cdot \left(-\frac{\mathrm{d}N_p}{\mathrm{d}z} \right) \cdot n_{Alk} = \frac{F}{z_0} e^{-z/z_0}. \tag{9}$$

As such, we get an exponentially declining alkalinity release profile when the particle volume is distributed according to an exponential distribution (depicted in Figure 1b). The exponential decline in alkalinity release is controlled by the reference parameter z_0, the penetration depth of particles with reference radius R. The alkalinity release at the surface is equal to that of the uniform particle profile.

2.2 Alkalinity release in the ocean mixed layer

The fraction χ of alkalinity that is released in the mixed layer can be calculated by integrating the alkalinity release profile down to the mixed layer depth (MLD), divided by the total alkalinity release per area and time, F. For the uniform particle profile (Equation 6), the fraction dissolving in the mixed layer is given by

$$\chi = \begin{cases} MLD/z_0 & \text{for } MLD \leq z_0 \\ 1 & \text{for } MLD > z_0\,. \end{cases} \tag{10}$$

For a uniform particle flux, χ can also be calculated from the residence time of the particles in the mixed layer t_{MLD} and the fraction of alkalinity released during this time as $\chi(t_{\text{MLD}}) = 1 - R^3(t_{\text{MLD}})/R^3(0)$ based on the shrinking core model (Köhler et al., 2013; Renforth and Kruger, 2013; Yang et al., 2025). t_{MLD} is then determined using the simplifying assumption that the particles do not shrink while in the mixed layer, such that $t_{\text{MLD}} = \frac{MLD}{v_{\text{sink}}(R(0))}$. This assumption is made since calculating the exact value of t_{MLD} would require to solve

$$\int_0^{t_{\text{MLD}}} v_{\text{sink}}(R(t))\mathrm{d}t = MLD \tag{11}$$

https://doi.org/10.5194/egusphere-2025-5917
Preprint. Discussion started: 8 December 2025

for t_{MLD} (with $v_{\mathrm{sink}}(R(t))$ given by Equations 2 and 4), requiring to find the roots of a third-order polynomial. However, by using $\chi(t_{\mathrm{MLD}}) = MLD/z_0$ as proposed here (Equation 10), one obtains the same third-order polynomial in t_{MLD} as obtained from the exact integral expression above, and thus the same mixed layer residence time.

For the exponential PSD profile (Equation 9), integrating the alkalinity release profile down to the MLD and normalizing by F results in

$$\chi = 1 - \exp\left(-MLD/z_0\right). \tag{12}$$

2.3 Variation of alkalinity release profiles with environmental conditions

The analytical alkalinity release profiles from sections 2.1.2 and 2.1.3 make the assumption of constant environmental conditions throughout particle dissolution. In the ocean, however, temperature and pH typically decrease with depth. A decrease in temperature (T) reduces the area-normalized dissolution rate r (Hangx and Spiers, 2009; Rimstidt et al., 2012), which, to a lesser extent, is countered by an increase in the dissolution rate from the co-occurring decrease in pH. In addition, a reduction in temperature will also increase dynamic viscosity, reducing the particles' sinking velocity. The impact of vertical temperature and pH variations on alkalinity release is further discussed in section 4.2.

To obtain simple analytical alkalinity release profiles, in particular for non-uniform PSDs, we here use vertically averaged temperature and pH to determine the reference depths z_0 for the dissolution profiles. However, z_0 depends on the vertical range over which the mean temperature and pH are determined. For example, using average conditions over the upper 100 m will result in higher dissolution rates and a shallower reference depth z_0 than using average conditions over the upper 1000 m, due to the colder temperatures in the ocean interior. The former would be more appropriate for smaller particles that dissolve close to the surface while the latter would be more appropriate for larger particles. To take into account that larger particles experience colder temperatures (and a often lower pH), we calculate the reference depth z_0 from Equation 5 with the mean conditions in temperature and pH between the surface and the reference depth itself ($\overline{T}_{0\to z_0}$ and $\overline{\mathrm{pH}}_{0\to z_0}$). In other words, z_0 is calculated self-consistently with mean conditions in temperature and pH over the same vertical range. To do so, we solve

$$z_0 = f(r(\overline{T}_{0\to z_0}, \overline{\mathrm{pH}}_{0\to z_0}), \mu(\overline{T}_{0\to z_0})), \tag{13}$$

numerically for z_0. Following this approach, a particle that dissolves close to the surface (small z_0) is modeled to dissolve under a warmer average temperature than a particle that penetrates the colder deep ocean (large z_0).

2.4 Experimental design with GFDL-ESM2M

In this study, we use the Earth system model GFDL-ESM2M to determine OAE efficiency for the here developed alkalinity release profiles. GFDL-ESM2M (Dunne et al., 2012, 2013) is a fully coupled carbon-climate Earth system model from NOAA GFDL, which contributed to the Coupled Model Intercomparison Project phase 5 (CMIP5). Its ocean component MOM4p1 (Griffies, 2009) uses a horizontal grid with 1° nominal resolution and 50 vertical layers with 10 m vertical resolution in the upper ocean. Ocean biogeochemistry is simulated by the Tracers of Ocean Phytoplankton with Allometric Zooplankton version

https://doi.org/10.5194/egusphere-2025-5917
Preprint. Discussion started: 8 December 2025

two (TOPAZv2 Dunne et al., 2013), and carbonate chemistry follows the OCMIP2 recommendations (Najjar and Orr, 1998) with air-sea CO_2 exchange determined by the bulk parameterization by Wanninkhof (1992).

As a first step, the reference depth parameter z_0 is calculated for forsterite (the most common form of olivine) for three different radii, $R = 0.86\,\mu$m, $R = 1.29\,\mu$m, and $R = 1.72\,\mu$m, with environmental conditions from GFDL-ESM2M. The three radii were selected to show the transition from shallow to deep particle penetration depth. z_0 is calculated for each vertical column of the ocean model grid separately, based on temporally averaged temperature and pH profiles over the period 2016-2025 and for 5 ensemble members (50 years in total). The period 2016-2025, extending an emission-driven historical simulation (Lacroix et al., 2024), is forced with Global Carbon Budget CO_2 emissions over 2016-2020 extended with NDCs for 2021-2025 (Friedlingstein et al., 2020), and non-CO_2 forcing as well as landuse changes prescribed from RCP2.6 (Van Vuuren et al., 2011). Since z_0 is determined in a fixed time-period, the impact of climate change on the dissolution profiles is not considered here. We take the area-normalized dissolution rate of forsterite for geometric surfaces as a function of temperature and pH from Rimstidt et al. (2012), also validated in Oelkers et al. (2018) and Fuhr et al. (2022) (see Appendix Figure A2). Dynamic seawater viscosity as a function of temperature is interpolated from the tabulated data in The Engineering ToolBox (2005). Forsterite density is taken from Anthony et al. (2001) and seawater density is set to global surface ocean conditions of $T = 18$°C and $S = 35$ PSU (The Engineering ToolBox, 2005). Variations in seawater density are negligible for particle sinking velocity since they are small compared to the density difference between the mineral particles and seawater. Alkalinity release that is prescribed below the ocean bottom cell is added to the bottom cell.

Based on the spatially-varying reference depths for the three radii and the two alkalinity release profile types (uniform particles and exponential PSD), we run six OAE experiments with differing alkalinity release profiles in GFDL-ESM2M. Following the CDRMIP protocol, alkalinity is continuously added to the global ocean between 60°S and 70°N, totaling to 0.14 Pmol alkalinity per year (Keller et al., 2018). For each of the six OAE experiments, GFDL-ESM2M is run over the period 2026-2200, under a CO_2 emission trajectory that stabilizes at 2°C global warming relative to the preindustrial period in absence of OAE (based on the AERA protocol; Terhaar et al., 2022; Silvy et al., 2024). These six simulations are compared to a simulation where alkalinity is added at the ocean surface. For the uniform alkalinity release profiles with $R = 1.29\,\mu$m and $R = 1.72\,\mu$m, we ran four additional ensemble members for the period 2026-2035 to analyze the role of internal variability over the first ten years of OAE. The simulations are run with interactive atmospheric CO_2 rather than prescribed concentrations. Thus, the OAE efficiency, calculated as the difference between air-sea carbon uptake in the OAE experiment and that in the baseline simulation, includes carbon cycle feedbacks between ocean, atmosphere, and land biosphere. This net ocean capture efficiency including the carbon cycle feedbacks is lower than the theoretically achievable gross efficiency of 0.8-0.85 without the adjustments in natural carbon reservoirs (Grosselindemann et al., in prep).

https://doi.org/10.5194/egusphere-2025-5917
Preprint. Discussion started: 8 December 2025

3 Results

3.1 Regional variation in alkalinity release

The reference depth z_0, calculated from Equations 5 and 13, increases strongly with particle size (Figure 2a-c). Globally averaged, z_0 values are 165 m, 638 m, and 1945 m for particle radii of $R = 0.86\,\mu$m, $R = 1.29\,\mu$m, and $R = 1.72\,\mu$m, respectively. Thus, doubling the radius from $R = 0.86\,\mu$m to $R = 1.72\,\mu$m increases z_0 by about a factor of twelve. Under constant environmental conditions, Equation 5 predicts a scaling of $z_0 \propto R^3$, corresponding to an eightfold increase. The stronger increase in z_0 arises from overall cooler conditions experienced by larger particles that sink deeper into the water column as discussed in Section 2.3.

The reference depth shows a pronounced latitudinal gradient (Figure 2a-c). It is substantially greater at high latitudes than at low latitudes. For example, for $R = 1.29\,\mu$m, the average reference depth increases from 367 m in the tropics (10°S-10°N) to 1043 m in the Southern Ocean (60°S to 45°S). This pattern arises primarily from lower water temperatures in high latitude regions, which suppress mineral dissolution rates and thereby increases reference depth. The effect of reduced dissolution is partially counteracted by the higher viscosity of colder waters, which slows particle sinking and limits penetration. However, the change in dissolution rate with temperature dominates: a 1°C cooling at 18°C results in a 9.2 % decrease in area-normalized dissolution rate, whereas viscosity increases only by 2.6 %. Latitudinal variations in pH exert a negligible impact on mineral dissolution rate (Appendix Figure A2). Even variations in pH of ± 0.1 alter z_0 by only a few meters.

Based on these reference depths, the fraction of alkalinity released within the annual maximum mixed layer can be calculated (Section 2.2, Figure 2d-i). Because waters above annual maximum MLD are well ventilated, alkalinity released in this layer directly contributes to oceanic carbon uptake. The fraction of alkalinity released in the mixed layer decreases with increasing particle size and is larger for the uniform particle profile than for the exponential profile, as larger particles in the latter are exported to greater depths. Globally, uniform particles with $R = 0.86\,\mu$m release 72 % of their alkalinity within the annual maximum mixed layer (Figure 2d), compared to 52 % for the exponential PSD profile with the same reference radius (Figure 2g). Increasing the reference radius to $R = 1.29\,\mu$m lowers the fraction to 20 % and 18 % for the uniform and exponential profile, respectively, and further to 6 % for both profiles at $R = 1.72\,\mu$m. For large reference radii, the reference depth is much larger than the mixed layer depth and the alkalinity release within the mixed layer between profiles is similar, because: $1 - \exp(-MLD/z_0) \approx MLD/z_0$ for $MLD/z_0 \ll 1$.

Regionally, alkalinity release in the mixed layer is large either where reference depths are shallow (low to mid-latitudes; Figure 2a-c) or where mixed layers are deep (e.g., western boundary current extension in the North Atlantic and North Pacific, the mode water formation regions of the Southern Ocean, and deep convection zones in the North Atlantic and Weddell Sea; Appendix Figure A3). Since regions are often either warm, associated with small reference depths, or have deep mixed layers, the latitudinal gradients of alkalinity release in the mixed layer are relatively small. For example, uniform particles with $R = 1.29\,\mu$m release 14 % of their alkalinity in the mixed layer in the tropics (10°S-10°N) and 20 % in the Southern Ocean (60°S to 45°S).

https://doi.org/10.5194/egusphere-2025-5917
Preprint. Discussion started: 8 December 2025

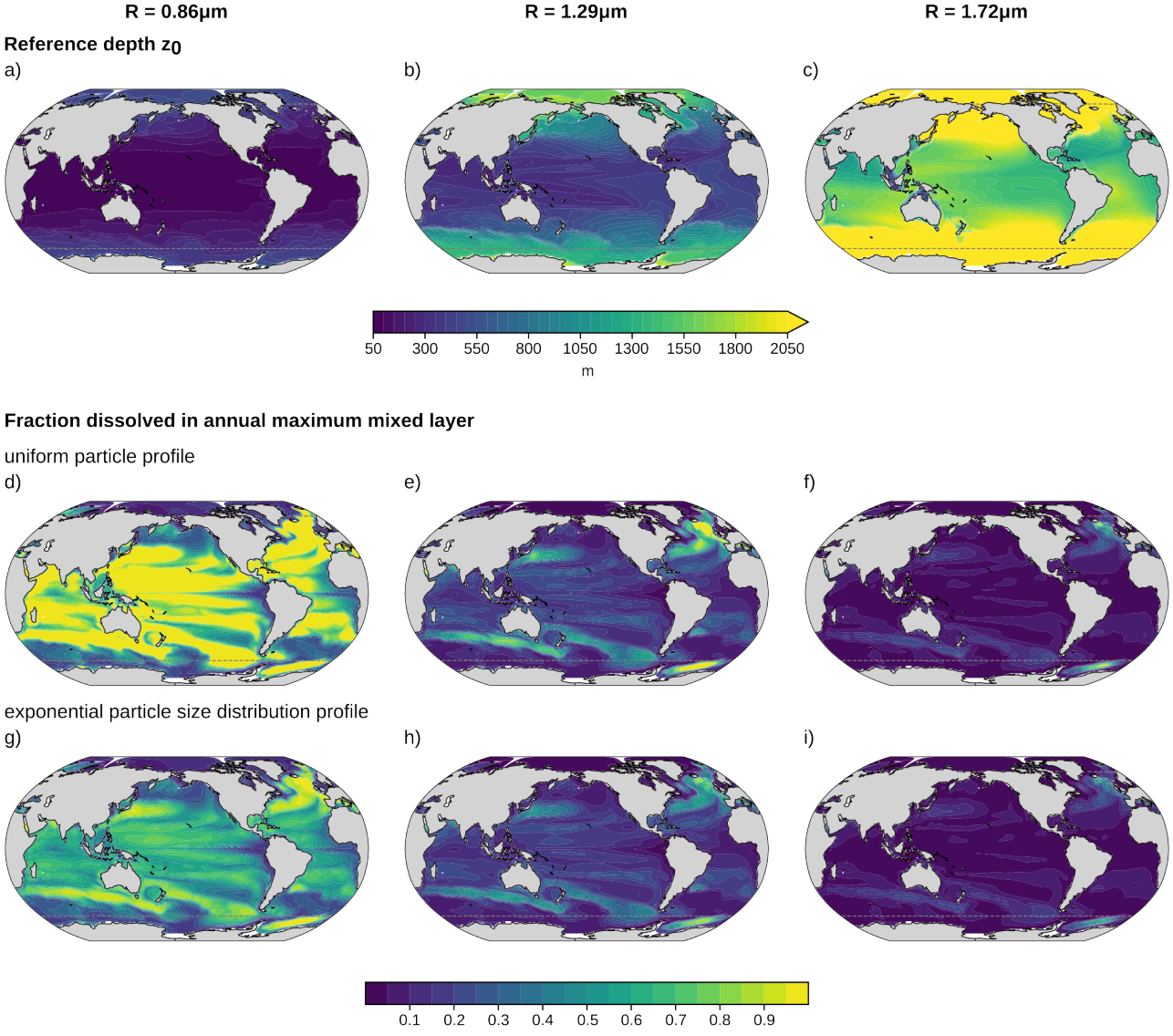

Figure 2. Regional variation in reference depth and mixed layer alkalinity release for particle radii $R = 0.86\,\mu$m (left column), $R = 1.29\,\mu$m (middle column), and $R = 1.72\,\mu$m (right column). (a-c) Reference depth determined with temperature and pH data from GFDL-ESM2M over the period 2016-2025 (see Sections 2.3 and 2.4). The fraction of alkalinity released above the annual maximum mixed layer depth (χ) for uniform particle profiles are shown in panels d-f and those for exponential particle size distribution profiles in panels g-i for each reference depth. The gray dashed lines enclose the region between 60°S and 70°N, where alkaline minerals are added to the surface ocean in this study.

https://doi.org/10.5194/egusphere-2025-5917
Preprint. Discussion started: 8 December 2025

3.2 Ocean carbon uptake and efficiency

Each profile type (uniform and exponential PSD) and particle size results in a characteristic vertical distribution of additional alkalinity relative to the reference simulation without OAE (Figure 3a). Averaged over 2026-2200, the additional alkalinity profile of the smallest reference radius R=0.86 μm, closely resembles that from surface dissolution, with only slightly lower concentrations close to the surface (57 μmol kg^{-1} for surface dissolution vs. 55 μmol kg^{-1} and 52 μmol kg^{-1} for the uniform and exponential PSD profiles, respectively). With increasing particle radius, additional alkalinity accumulates at larger depths. This is particularly the case for the exponential PSD profile, where 37 % of the alkalinity is released below z_0 compared to no release below z_0 for the uniform profile (global mean values for z_0 are shown as dashed lines in Figure 3a). As a result, additional alkalinity near the surface declines. For R=1.72 μm, additional surface alkalinity reduces to 21 μmol kg^{-1} and 18 μmol kg^{-1} for the uniform and exponential PSD profiles, respectively.

Relative to surface alkalinity release, this deeper alkalinity release reduces OAE capture efficiency, defined as the ratio of additional carbon uptake to the alkalinity added (Figure 3b). The reduction is most pronounced in the first decades of continuous alkalinity addition. Over the first 30 years, efficiency decreases by more than two thirds for R=1.72 μm, to 0.20 and 0.18 mol C_T (mol A_T)$^{-1}$ when alkalinity is released according to the uniform and exponential PSD profiles, respectively, compared to 0.65 mol C_T (mol A_T)$^{-1}$ for surface dissolution and alkalinity release. For the intermediate reference radius R=1.29 μm, efficiency is reduced to 0.44 mol C_T (mol A_T)$^{-1}$ (-32 %) and 0.39 mol C_T (mol A_T)$^{-1}$(-40 %) for the uniform and exponential PSD profiles, respectively. For the exponential PSD profile with the smallest reference radius R=0.86 μm, we find a 16 % decrease in efficiency to 0.54 mol C_T (mol A_T)$^{-1}$. Efficiency is further reduced during the first decade with 0.32 and 0.14 mol C_T (mol A_T)$^{-1}$ for uniform particles with $R = 1.29$ and 1.72 μm, respectively, compared to 0.65 mol C_T (mol A_T)$^{-1}$ for surface dissolution. As such, efficiency decreases by more than 75 % over the first ten years for particles with 1.72 μm radius.

Over time, the difference in efficiency relative to surface alkalinity release becomes smaller, reflecting the gradual transport of alkalinity released at depth back to the surface. Nevertheless, the average efficiency over 2026-2200 remains less than half of that of surface addition for R=1.72 μm (0.29 and 0.25 mol C_T (mol A_T)$^{-1}$, respectively, compared to 0.60 mol C_T (mol A_T)$^{-1}$). Year-to-year variability in OAE efficiency is substantial in all experiments (standard deviation around 0.18 mol C_T (mol A_T)$^{-1}$); thin lines in Figure 3b). These strong fluctuations in carbon uptake mainly arise because we run the experiments in a fully coupled Earth system model, where natural variations in air-sea CO_2 flux in the OAE experiment and the baseline simulation are superimposed onto the carbon uptake signal from OAE. This would not be the case in ocean-only model experiments. However, the uncertainty in the additional carbon flux due to OAE is also larger when alkalinity is released in the ocean interior instead of at surface. For larger particle sizes, the variability in OAE-induced carbon uptake approaches the magnitude of the mean (coefficients of variation are 0.56 and 0.72 for the uniform and exponential PSD profiles with $R = 1.72\,\mu$m). Thus, ocean circulation variability adds further uncertainty to monitoring OAE efficiency when alkalinity is released along vertical profiles.

https://doi.org/10.5194/egusphere-2025-5917
Preprint. Discussion started: 8 December 2025

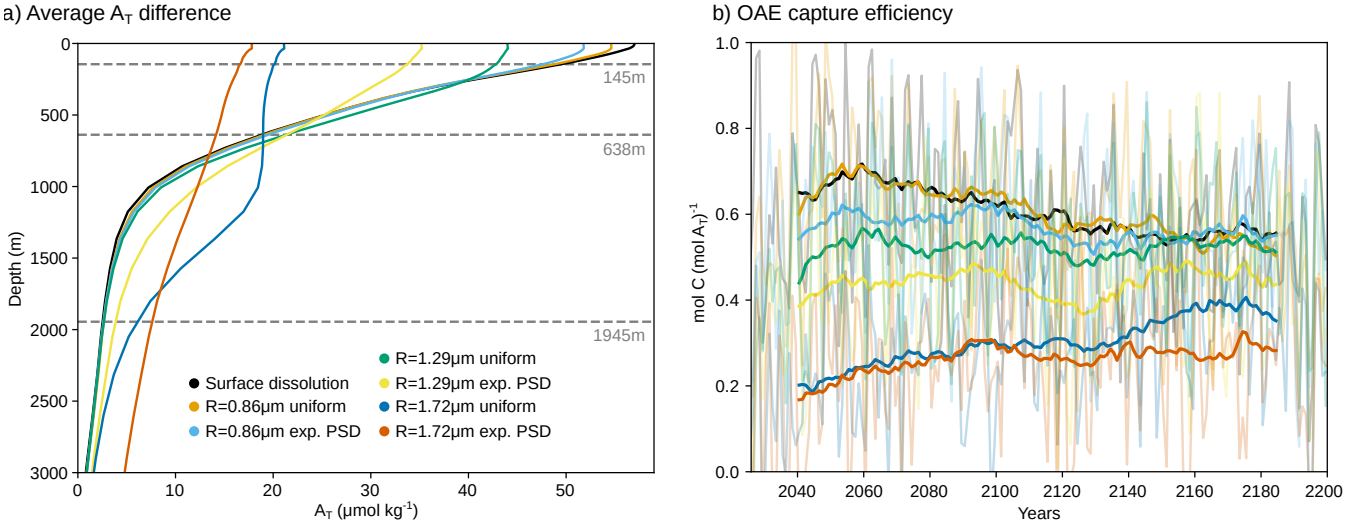

Figure 3. (a) Global mean difference in total alkalinity between the OAE simulations for surface dissolution and uniform as well as exponentially distributed particle size distributions and the baseline simulation without OAE, averaged over 2026-2200. Dashed lines indicate the global mean reference depths z_0 for the three reference radii R=0.86 μm, R=1.29 μm, and R=1.72 μm. (b) The OAE efficiency for these simulations over time, defined as the number of moles of additional carbon uptake in the OAE simulations divided by the number of moles alkalinity added. Light colors indicate annual average values and dark colors show 31-year running means.

During the first ten years of alkalinity addition, OAE with vertical alkalinity release profiles results in additional carbon uptake relative to the baseline simulation without ocean alkalinity enhancement over most of the ocean (see Figure 4a for the additional CO_2 uptake for uniform particles with radius $R = 1.29\,\mu$m). However, carbon uptake and efficiency are generally lower than when alkalinity is released directly at the surface (Figure 4c). As expected, regions with particularly low alkalinity release in the mixed layer (Figure 2e) partially overlap with regions of low carbon uptake (Figure 4a), such as in the northern and eastern North Pacific or the Atlantic section of the Southern Ocean. Carbon uptake is higher in the Kuroshio current extension, the Gulf Stream region in the North Atlantic, and mode water source regions on the Southern Ocean, where the fraction of alkalinity release in the mixed layer is also relatively high. However, despite relatively low alkalinity release in the mixed layer, the tropical upwelling regions show considerable carbon uptake, which may indicate the upwelling of alkalinity back to the surface. Overall, the fraction of alkalinity release in the annual maximum mixed layer only partially explains the regional variations in carbon uptake even on short timescales such as ten years. The pattern correlation between the fraction of alkalinity release in the mixed layer and OAE-induced carbon uptake for $R = 1.29\,\mu$m particles, averaged over the 5 ensemble members, is only 0.34 between 60°S and 70°N. However, the carbon uptake pattern also varies strongly among the five ensemble members. We analyze this by calculating the pattern correlation coefficients between the carbon uptake patterns of the different ensemble members over the first ten years of experiment. The mean of the ten pairwise pattern correlation coefficients

https://doi.org/10.5194/egusphere-2025-5917
Preprint. Discussion started: 8 December 2025

across the five ensemble members is 0.15 and 0.37 for uniform $R = 1.72\,\mu$m and $R = 1.29\,\mu$m particles, respectively. As such, regional carbon uptake is more uncertain for larger particles where alkalinity is released deeper in the water column.

At longer timescales, ocean carbon uptake increases in regions with deep mixed layers (cf. Figure 4b and Appendix Figure A3), in the upwelling region of the tropical Pacific, as well as in Eastern Boundary upwelling systems (Figure 4b). The increase in carbon uptake in these regions suggests that additional alkalinity released at subsurface in other regions is transported there, where it comes in contact with the atmosphere. As these waters with additional alkalinity have not yet equilibrated with the atmosphere, additional carbon is taken up. As a result, carbon uptake becomes larger than in the simulation with direct alkalinity addition at the surface in these regions (Figure 4d). Increased carbon uptake is also observed south of 60°S where no alkalinity is added, indicating an increased southward transport of alkalinity from regions North of 60°S when alkalinity is released at subsurface. Yet, carbon uptake remains lower over most of the low-to-mid latitudes, such that global carbon uptake remains 16 % lower than when alkalinity is added to the surface (Figure 3b).

4 Discussion

4.1 Comparison to earlier studies

Our study suggests a shallower release of alkalinity compared to Köhler et al. (2013), who estimated that about 80 % of alkalinity from forsterite olivine particles with a 0.5 μm radius is released within the maximum mixed layer. Repeating the analysis from section 3.1 for particles of 0.5 μm radius, we find a release of 98 % in the annual maximum mixed layer. The shallower release of alkalinity in our study primarily arises from the higher area-normalized dissolution rate adopted here, based on geometric surfaces from Rimstidt et al. (2012). For example, the dissolution rate is 84 % higher at 25 °C than the rate from Hangx and Spiers (2009) used in Köhler et al. (2013). A secondary contribution stems from the deeper maximum MLD in our model, 123 m on global average (34 m deeper than observations; Dunne et al., 2012), compared to 64 m in Köhler et al. (2013). As the dissolution rate from Rimstidt et al. (2012) has been validated against observations in multiple studies (Oelkers et al., 2018), the mixed layer alkalinity release fractions obtained here are likely more robust. Nonetheless, the comparison underscores the strong sensitivity of vertical alkalinity release to the assumed mineral dissolution rate. Despite the shallower release, the spatial patterns of mixed layer alkalinity release are broadly consistent with those of Köhler et al. (2013) (cf. Figure 2 and their Figure 3d).

Our results are also qualitatively consistent with Fakhraee et al. (2023), who modeled alkalinity release using a more complex mineral particle model that includes particle aggregation and zooplankton interaction. Their study employed an experimental PSD from Renforth (2012), in which 80 % of particle mass is contained in particles smaller than 10 μm in diameter (radius less than 5 μm). To enable comparison, we discretize the experimental PSD into 14 discrete size classes and convert the experimentally determined mass fractions per size class into particle number fractions (see Appendix section A and Figure A5a). The resulting cumulative alkalinity release profiles (Figure A5b) are qualitatively similar to those reported by Fakhraee et al. (2023) though our model predicts a shallower release. While Fakhraee et al. (2023) found 25 % to 45 % of alkalinity release in the upper 80 m, with increased release for higher feedstock application rates, we obtain 54 % to 61 % for temperatures

https://doi.org/10.5194/egusphere-2025-5917
Preprint. Discussion started: 8 December 2025

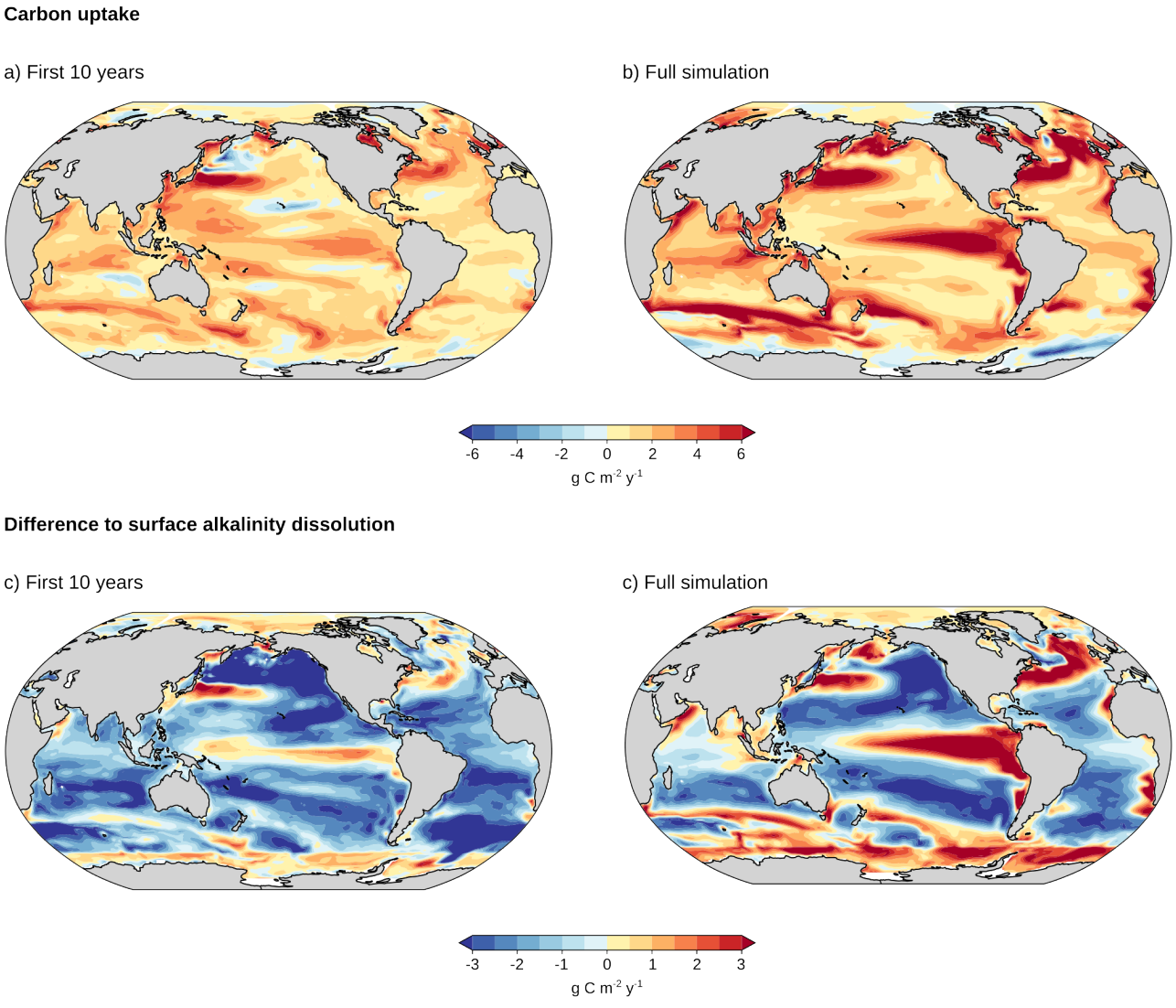

Figure 4. Regional carbon uptake for the OAE experiment with uniform particles of radius R=1.29 μm relative to the baseline simulation without ocean alkalinity enhancement over (a) the first 10 years (2026-2035), averaged over five ensemble members to increase robustness, and (b) the over the full simulation (2026-2200). The difference between the carbon uptake for this uniform particle size and that for surface alkalinity addition is shown in panels c) for the first ten years and d) for the full period.

https://doi.org/10.5194/egusphere-2025-5917
Preprint. Discussion started: 8 December 2025

of 10°C to 25°C. This difference suggests that including particle aggregation and zooplankton interactions, as in Fakhraee et al. (2023), may further reduce the efficiency of ocean alkalinity enhancement.

4.2 Limitations of the analytical shrinking core treatment of mineral particles

The analytical framework presented here involves several simplifying assumptions. The main limitations concern (i) the idealized representation of particle geometry and sinking, (ii) the omission of particle interactions with the environment such as aggregation, scavenging, or the formation of coating layers, (iii) the use of mean rather than depth-resolved environmental conditions, and (iv) the omission of particle advection during dissolution.

First, the shrinking core model assumes smooth, spherical particles, thereby neglecting variations in grain shape and surface roughness. To account for the larger microscopic surface of non-spherical particles, we use the area-normalized dissolution rate for geometric spherical surfaces, which is larger than for microscopic surfaces (Rimstidt et al., 2012). Non-spherical shapes and surface roughness could also reduce particle sinking velocities, whereas fluid instabilities during particle sinking could enhance the sinking velocity (Yang and Timmermans, 2024; Yang et al., 2025). As a result, the depth of alkalinity release in the ocean may be deeper than simulated here. For example, Yang et al. (2025) estimate that the fraction of alkalinity released within the mixed-layer decreases from 7.3 % to 0.4-1.5 % when accounting for such instabilities rather than assuming Stokes' sinking velocity.

Second, we also neglect potential particle interactions with the environment. Smaller mineral particles may aggregate, forming larger particles that sink faster (Köhler et al., 2013). Mineral particles may also attach to biogenic particles through scavenging or zooplankton ingestion, suppressing near-surface alkalinity release (Fakhraee et al., 2023). Mineral or microbial coating layers may form on the particles' surfaces (Wang and Giammar, 2013; Oelkers et al., 2018), which can reduce the contact area with the surrounding water and mineral dissolution.

Third, to obtain analytical alkalinity release profiles, we assume that dissolution occurs at the mean temperature and pH between surface and reference depth z_0 (Section 2.3). This simplification neglects vertical and seasonal gradients that could enhance dissolution in warmer surface waters and reduce it at depth. The approximation performs best where such gradients are small (e.g., at high latitudes or for shallow-sinking particles). For instance, in a subtropical Atlantic column with a 9.2 °C temperature range between surface and a particle's penetration depth of 300 m, surface alkalinity release is 27 % higher and deep release is 28 % lower than predicted using mean conditions, whereas in the Southern Ocean (1.8 °C range) the differences are only 9 % and 2 %, respectively (Fig. A4a,b). The stronger mismatch at low latitudes thus reflects the larger vertical temperature contrast. The use of mean environmental conditions to determine a particle's reference depth also neglects the nonlinear dependence of dissolution rate on temperature and pH (Rimstidt et al., 2012). Because the dissolution rate is a convex function of these variables, the rate at vertically averaged conditions is slightly lower than the average rate computed over the full profile, resulting in a deeper predicted penetration depth. The effect is generally small: across the global ocean, reference depths differ by less than 10 % over 90 % of the area for 1.29 μm particles (Fig. A4d). For these particles, explicit profiles yield a globally averaged reference depth that is only 14 m shallower than the idealized case, though mixed-layer release fractions increase by about 6 % (a relative rise of 28 %, Fig. A4f). Hence, while vertically resolved profiles yield higher

https://doi.org/10.5194/egusphere-2025-5917
Preprint. Discussion started: 8 December 2025

surface release, the idealized treatment remains a good first-order approximation. For the exponential PSD profile, we also assume that all particle sizes experience identical mean temperature and pH, although larger particles typically penetrate into colder, more acidic waters than smaller ones. Accounting for these variations would increase the spread in penetration depth across the PSD, resulting in a deeper alkalinity export for larger particles.

Fourth, the present framework neglects the horizontal and vertical advection of mineral particles during dissolution. Because dissolution can span several years (Appendix Figure A1a), advection of mineral particles in the subsurface may modify the depth and spatial patterns of alkalinity release. This aspect should be assessed in subsequent studies.

Overall, these simplification may lead to a modest underestimation of mineral export and deep alkalinity release, primarily due to enhanced sinking velocities in presence of fluid instabilities (Yang and Timmermans, 2024; Yang et al., 2025), particle aggregation (Fakhraee et al., 2023) and the possible formation of coating layers on the particles (Oelkers et al., 2018). Nevertheless, the simplified vertical profiles developed here capture the first-order effects of environmental conditions and feedstock properties on alkalinity release, providing a robust basis for sensitivity analyses of ocean alkalinity enhancement efficiency.

4.3 Implications for feasibility of open-ocean mineral-based OAE

Our study confirms that olivine must be milled to grain sizes (particle diameters) near 1 μm to achieve feasible carbon removal through open-ocean alkalinity enhancement (Köhler et al., 2013; Boyd and Vivian, 2019). When particles are uniformly milled to a radius of 0.86 μm radius (1.72 μm diameter), carbon capture efficiency remains comparable to that of instantaneous surface dissolution. In contrast, doubling the radius to 1.72 μm (3.44 μm diameter) reduces the efficiency to less than one third within the first decades.

Olivine powder with the same mean particle volume as 0.86 μm radius particles but with an exponential particle-size distribution marks a transition between near-optimal and considerably reduced capture efficiency. In this case, efficiency is 16 % lower than with direct surface alkalinity addition over the first three decades, with full efficiency reached only by the end of the 21st century (Figure 3b). These long timescales until full efficiency result from an overproportionally larger fraction of alkalinity stored in the larger particles that sink deeper. While 80 % of particles are smaller than 1 μm, they only contain 48 % of the alkalinity. In contrast, the largest 0.3 % of particles in the PSD, exceeding 1.55 μm, still contain 2 % of the alkalinity. In natural or industrially milled powders, more heavy-tailed PSDs can further exacerbate this problem. For example, in the experimental PSD from Renforth (2012), 73 % of the alkalinity resides in the largest 0.3 % of particles, resembling a power law distribution (Figure A5a). For this heavy-tailed PSD, 20 % of the alkalinity is contained in particles with diameters larger than 10 μm, compared to only 2.5 μm for the exponential PSD, despite a smaller mean particle size in the experimental PSD. Thus, beyond minimizing mean particle size, achieving a rapid decay of particle abundance at larger sizes is essential for efficient OAE.

The strong dependence of carbon capture efficiency on the particle size distribution underscores a fundamental trade-off between particle fineness and energy demand. Producing micrometer-scale olivine particles greatly increases comminution energy and associated life-cycle emissions. Foteinis et al. (2023) estimated that the life-cycle emissions for 1 μm are more than four times larger than for 10 μm particles. This trade-off calls into question the feasibility of olivine-based OAE for the

https://doi.org/10.5194/egusphere-2025-5917
Preprint. Discussion started: 8 December 2025

open-ocean, although olivine may remain suitable for coastal applications where the mixed layer extends to the seafloor, such that alkalinity release from the sediments enhances carbon uptake from the atmosphere (Renforth, 2012; Montserrat et al., 2017; Foteinis et al., 2023).

Alternative alkaline materials with higher dissolution rates, such as brucite, may relax the particle-size constraints. Using Equation 5, one can calculate the permissible increase in mean particle volume for a more quickly dissolving material (indicated by primes) such that the reference depth stays constant:

$$\frac{V'_R}{V_R} = \frac{r'}{r} \cdot \frac{V'_m}{V_m} \cdot \frac{\rho_p - \rho_w}{\rho'_p - \rho_w} \tag{14}$$

Because brucite dissolves roughly 100 times faster than forsterite at $T = 25°C$ and pH=8 (Pokrovsky and Schott, 2004), the allowable particle volume increases by a factor of 90, corresponding to an increase in radius by a factor of 4.5. Thus, an exponential PSD with reference radius of R=0.86 μm for forsterite corresponds to an equally efficient PSD with a reference radius of R=3.9 μm for brucite.

The framework developed here can be generalized to other PSDs by deriving corresponding vertical alkalinity release profiles, as illustrated for the exponential and discrete PSDs. This approach provides a direct estimate of the alkalinity released within the mixed layer (Section 2.2), improving on earlier approaches assuming constant sinking velocity in the mixed layer (Renforth and Kruger, 2013; Köhler et al., 2013; Yang et al., 2025). Our Earth system model simulations indicate, however, that regional variation in oceanic carbon uptake is only partly explained by mixed-layer dissolution. The remaining differences highlight the role of ocean circulation and alkalinity redistribution, which can only be captured with ocean-biogeochemical models.

Such ocean-biogeochemical models are also essential for assessing how mineral OAE with subsurface alkalinity release affects ocean acidification (OA). Relative to surface dissolution, and averaged over 2026-2200, mineral OAE with an exponential PSD and a 1.72 μm reference radius results in a 0.015 unit lower pH (weaker OA mitigation) in the upper 482 m of the water column, and a 0.015 unit higher pH (stronger OA mitigation) at greater depths (Appendix Figure A6c). Notably, OA mitigation is increased below 482 m even though the alkalinity enhancement is smaller than under surface dissolution down to 792 m (Figure 3a). This occurs because waters contain lower dissolved inorganic carbon concentrations as a result of the lower ocean carbon uptake under subsurface alkalinity addition. Overall, these results indicate a downward shift in the depth of OA mitigation and an enhanced mitigation potential driven by the reduced carbon uptake and efficiency of the mineral-based OAE.

5 Conclusions

In summary, the efficiency of mineral-based open-ocean alkalinity enhancement and associated CO_2 uptake is highly sensitive to feedstock particle-size characteristics. Inefficient comminution or heavy-tailed particle-size distributions can substantially reduce carbon capture efficiency and delay CO_2 uptake by decades to centuries, often shifting it far from the deployment site. Such temporal and spatial lags complicate monitoring, reporting and verification and challenge carbon crediting schemes

https://doi.org/10.5194/egusphere-2025-5917
Preprint. Discussion started: 8 December 2025

based on short-term removal. Our findings emphasize the need for integrated process–energy–climate assessments to evaluate the feasibility of large-scale, mineral-based ocean alkalinity enhancement.

Code and data availability. The code used for this study and the analyzed simulation data are available under the Zenodo repository ... (the link /DOI for the repository will be added at a later point in the review process).

Appendix A: Alkalinity release for the experimental PSD by Renforth (2012)

To derive an alkalinity release profile, we first discretize the particle size distribution from Table 1 in Renforth (2012) by assuming all particles within the 14 particle size intervals to have the respective mean diameters of the intervals $d_{i=1,..14}$. We then calculate the particle volume for each size class as $V_i = \frac{\pi d_i^3}{6}$. As a next step, the retained mass fractions m_i in each interval are transformed into number fractions n_i. With $V_{\mathbf{tot}} \cdot m_i/v_i$ the number of particles in size class i (V_{tot} is the total volume of all particles), the number fraction in size class i is given by

$$n_i = \frac{V_{\text{tot}} \cdot m_i/V_i}{\sum_i V_{\text{tot}} \cdot m_i/V_i} = \frac{m_i/V_i}{\sum_i m_i/V_i}.$$

The probability density function for these discrete number fractions n_i at volumes V_i is then given by

$$f(V) = \sum_i n_i \cdot \delta(V - V_i).$$

The reference volume, given by the mean particle volume of the distribution, is calculated as $V_R = \sum_i n_i V_i$. The corresponding reference depth z_0, the penetration depth for particles with reference volume V_R, is calculated according to Equation 5. The alkalinity release profile can now be calculated as done for the exponential PSD in Equation 9:

$$\begin{aligned}\frac{\mathrm{d}A_{\mathrm{T}}}{\mathrm{d}t}(z) &= \left(F_p \cdot \int_{V_{\min}(z)}^{\infty} f(V)\mathrm{d}V\right) \cdot \left(-\frac{\mathrm{d}N_p}{\mathrm{d}z}\right) \cdot n_{Alk} = F_p \left(-\frac{\mathrm{d}N_p}{\mathrm{d}z}\right) \cdot n_{Alk} \cdot \sum_i n_i \int_{V_{\min}(z)}^{\infty} \delta(V - V_i)\mathrm{d}V \\ &= F_p \left(-\frac{\mathrm{d}N_p}{\mathrm{d}z}\right) \cdot n_{Alk} \cdot \sum_i n_i \theta(V_i - V_{\min}(z)) = \frac{F}{z_0} \sum_i n_i \theta(V_i - V_{\min}(z)),\end{aligned}$$

with $V_{\min}(z)$, the minimum initial volume of a particle to still be present at depth z (Equation 8).

Finally, the fraction of alkalinity release between the surface and depth z is calculated by integrating the alkalinity release profile and normalizing by the surface alkalinity flux (see Section 2.2):

$$\frac{1}{F}\int_0^z \frac{\mathrm{d}A_{\mathrm{T}}}{\mathrm{d}t}(z)\,\mathrm{d}z = \frac{1}{z_0}\sum_i n_i \int_0^z \theta(V_i - V_{\min}(z))\,\mathrm{d}z = \frac{1}{z_0}\sum_i n_i \cdot \min(z, z_0 \frac{V_i}{V_R}).$$

In the last step, it was used that $\theta(V_i - V_{\min}(z))$ is zero if $V_i < V_{\min}(z)$, which is the case if $z > z_0 \frac{V_i}{V_R}$ (Equation 8).

https://doi.org/10.5194/egusphere-2025-5917
Preprint. Discussion started: 8 December 2025

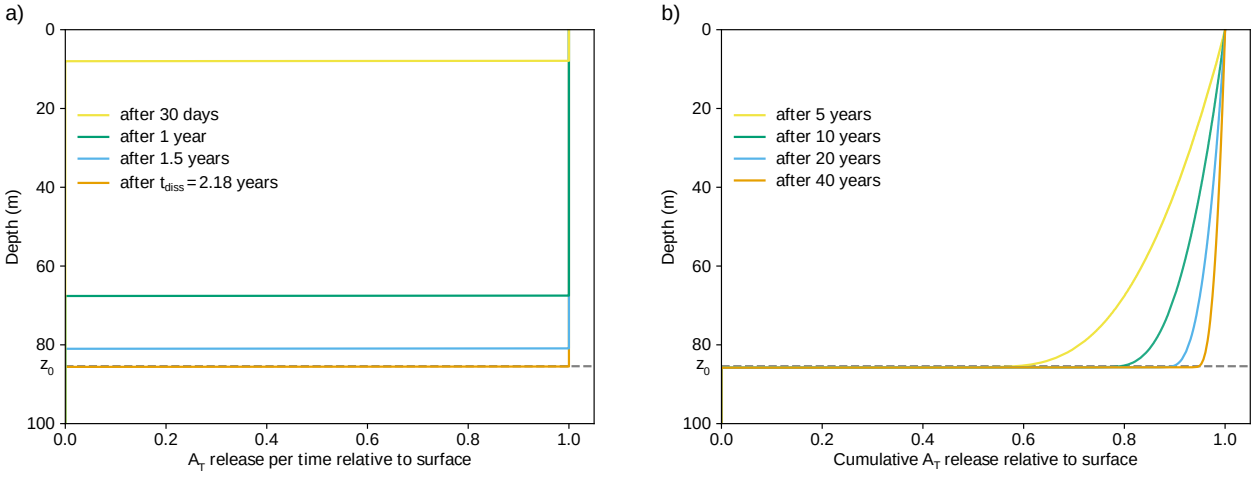

Figure A1. Numerical simulation used to validate the analytical uniform particle flux profile. Particles of radius $R = 0.86\,\mu$m are continuously added at the surface ($T = 25\,°$C, pH $= 8.2$) and sink through a vertical grid of 0.1 m resolution with a timestep of 1 h. (a) The alkalinity release in each time step at different time points. The release is constant with depth but only reaches down to the depth the first particle reached. At the dissolution time t_{diss} and afterwards, the alkalinity release profile extends down to the reference depth z_0. (b) The cumulative alkalinity release is not strictly rectangular, since particles that were released less than t_{diss}=2.18 years before have not reached z_0 yet and have only released alkalinity at shallower depths. For longer time periods since the start of the experiment, these particles matter relatively less, such that the cumulative alkalinity release is eventually also approximately rectangular. For example, the cumulative alkalinity released at depth z_0 is 95 % of that at the surface after 40 years.

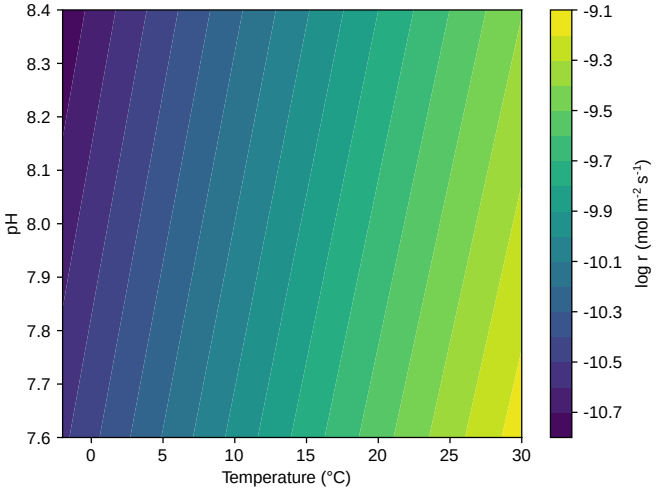

Figure A2. The base-10 logarithm of the area-normalized dissolution rate of forsterite from Rimstidt et al. (2012) as a function of temperature and pH.

https://doi.org/10.5194/egusphere-2025-5917
Preprint. Discussion started: 8 December 2025

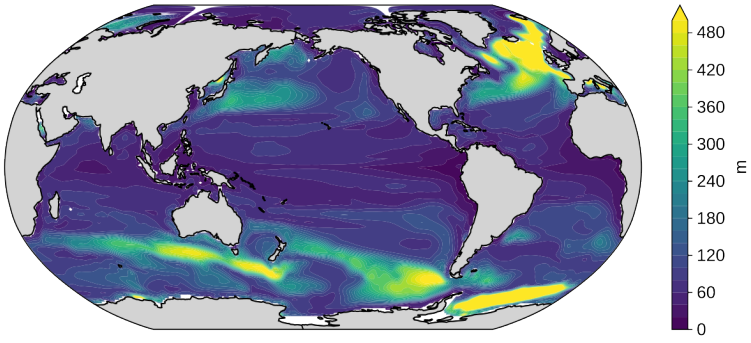

Figure A3. Annual maximum mixed layer depth in the GFDL-ESM2M model. Mixed layer depth is defined as the depth where density increases by 0.03 kg m^{-3} relative to the surface. It is calculated as the annual maximum of monthly mixed layer depth, averaged over the period 2016-2025 and over five ensemble members. Global average annual maximum mixed layer depth is 123 m.

https://doi.org/10.5194/egusphere-2025-5917
Preprint. Discussion started: 8 December 2025

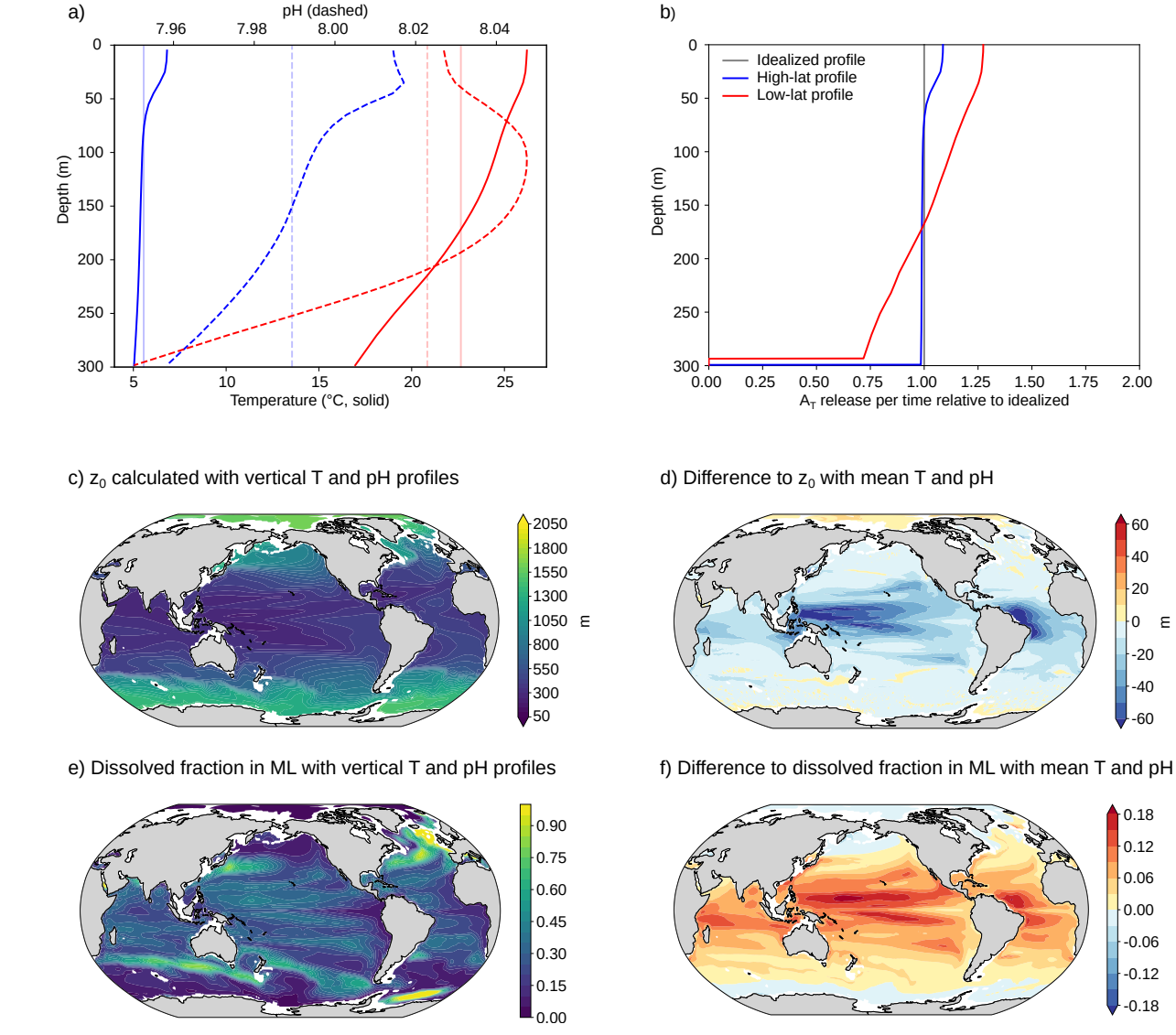

Figure A4. Numerical simulation used to test the influence of variations in temperature and pH along the water column on the alkalinity release profile. Panel a shows two exemplary temporal mean profiles, one from the Southern Ocean (-57.5°N, 177.5°E) in blue and one from the subtropical Atlantic (20.9°N, -58.5°E) in red. Light vertical lines in panel a show mean temperature and pH over the upper 300 m. Under the idealized dissolution profile approach (Section 2.3), particles with a radius of 0.86 μm in the subtropical Atlantic column and particles with a radius of 1.29 μm in the Southern Ocean column both penetrate down to 300 m (reference depth z_0 of 300 m). The numerical alkalinity release profiles with explicit vertical temperature and pH profiles are shown in panel b. Panel c shows the reference depth with explicit temperature and pH profiles for particles with radius r=1.29 μm globally, and panel d shows the difference to the reference depth assuming mean temperature and pH (Figure 2e). Regions where the water column is shallower than the reference depth are left blank as they do not allow a direct comparison. Panel e shows the fraction dissolved in the annual maximum mixed layer with explicit temperature and pH profiles and panel f shows the difference to the dissolved fraction assuming mean temperature and pH (Figure 2h).

https://doi.org/10.5194/egusphere-2025-5917
Preprint. Discussion started: 8 December 2025

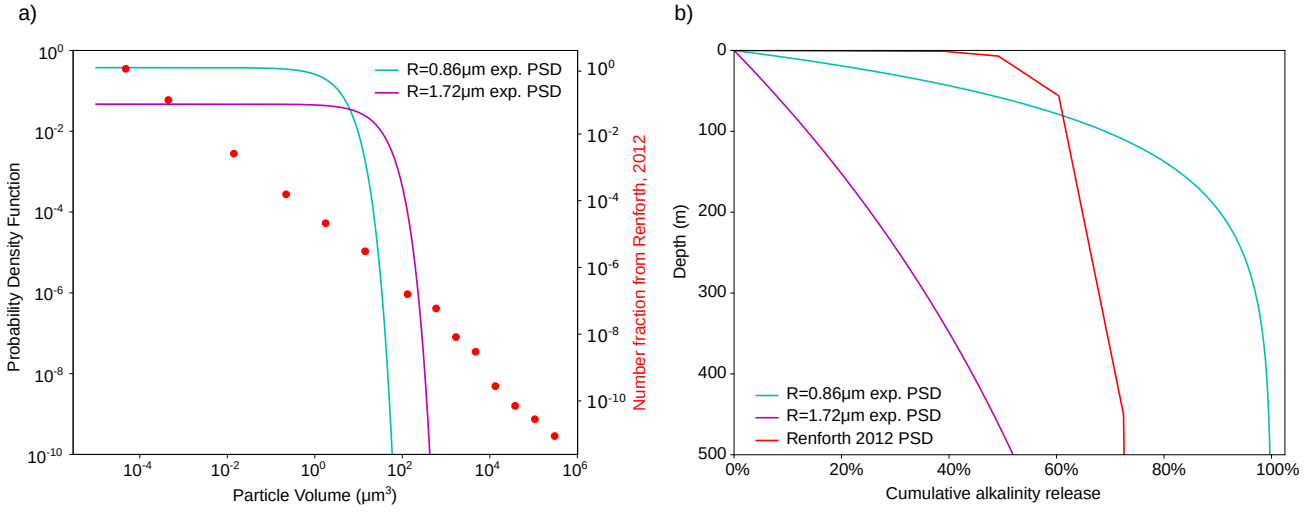

Figure A5. (a) Discretized sieve-based particle size distribution from Renforth (2012) compared to the exponential particle size distributions from this study for mean particle volumes corresponding to radii of 0.86 μm and 1.72 μm, respectively. The PSDs are plotted on a log-log scale as that from Renforth (2012) spans many orders of magnitudes in particle volume, with it's near-linear evolution resembling a heavy-tailed power-law distribution. (b) Cumulative alkalinity release over the upper 500 m assuming T=25°C and pH=8.2.

https://doi.org/10.5194/egusphere-2025-5917
Preprint. Discussion started: 8 December 2025

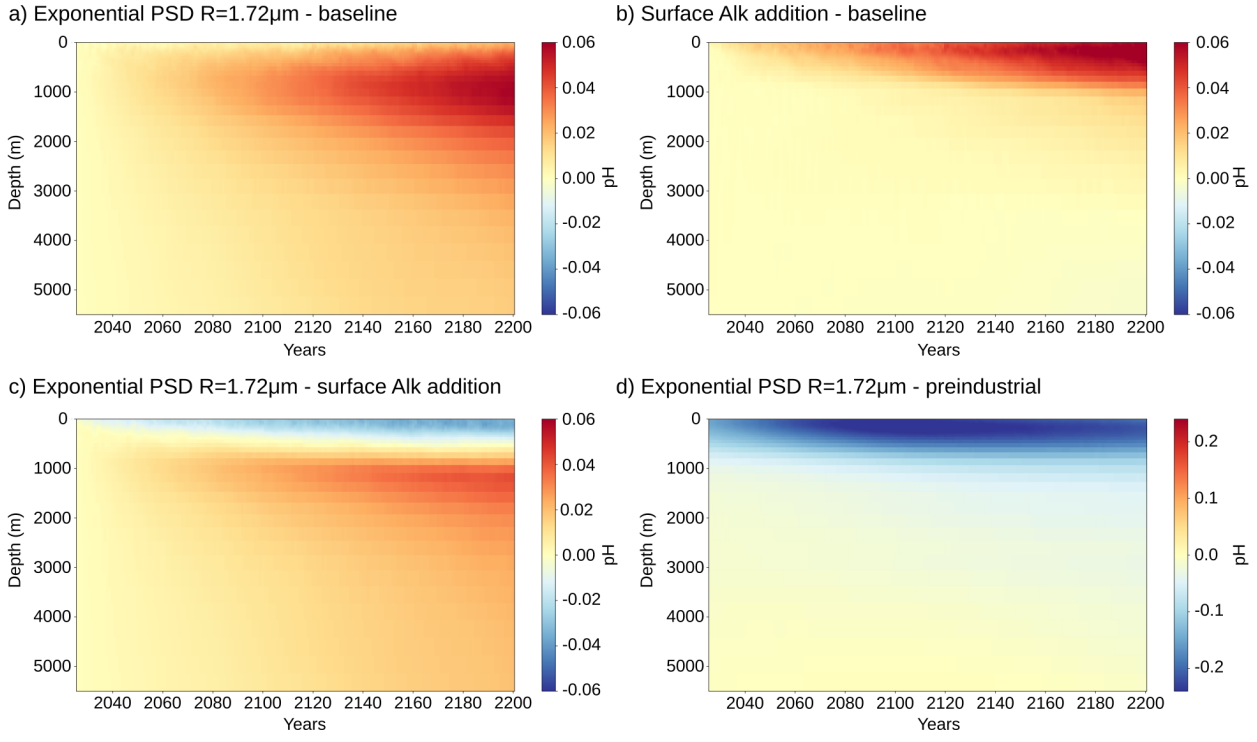

Figure A6. Global-mean pH difference along the water column between OAE and the baseline simulation without OAE, for (a) the exponential PSD with reference radius of 1.72 μm and (b) surface alkalinity addition. The pH change is averaged over the period 2026-2200. Panel c shows the pH difference between the exponential PSD with reference radius of 1.72 μm and surface alkalinity addition. Panel d shows the total change in pH from the baseline CO_2 emissions and OAE with the exponential PSD relative to the pre-industrial state.

https://doi.org/10.5194/egusphere-2025-5917
Preprint. Discussion started: 8 December 2025

Author contributions. The concept of the study and the methodology for the dissolution profiles were developed by F.A.B. U.H.E. and F.A.B. implemented the dissolution profile in the Earth system model. F.A.B. conducted the simulations with subsurface alkalinity addition and the baseline simulations without OAE. H.G. conducted the simulations with surface alkalinity addition. F.A.B., U.H.E., H.G., and T.F jointly worked on the interpretation of the results. The initial draft was written by F.A.B., and U.H.E., H.G., and T.F. provided feedback and revised the text.

Competing interests. The authors declare that they have no conflict of interest.

Acknowledgements. This study was supported by the Bloom Foundation. The authors also thank the CSCS Swiss National Supercomputing Centre for computing resources (project number s1328).

https://doi.org/10.5194/egusphere-2025-5917
Preprint. Discussion started: 8 December 2025

References

Anthony, J. W., Bideaux, R. A., Bladh, K. W., and Nichols, M. C., eds.: Handbook of Mineralogy, Mineralogical Society of America, Chantilly, VA 20151-1110, USA, http://www.handbookofmineralogy.org/, 2001.

Babiker, M., Berndes, G., Blok, K., Cohen, B., Cowie, A., Geden, O., Ginzburg, V., Leip, A., Smith, P., Sugiyama, M., and Yamba, F.: Cross-sectoral perspectives, in: Climate Change 2022: Mitigation of Climate Change. Contribution of Working Group III to the Sixth Assessment Report of the Intergovernmental Panel on Climate Change, edited by Shukla, P. R., Skea, J., Slade, R., Al Khourdajie, A., van Diemen, R., McCollum, D., Pathak, M., Some, S., Vyas, P., Fradera, R., Belkacemi, M., Hasija, A., Lisboa, G., Luz, S., and Malley, J., Cambridge University Press, Cambridge, UK and New York, NY, USA, https://doi.org/10.1017/9781009157926.005, 2022.

Boyd, P. W. and Vivian, C.: High level review of a wide range of proposed marine geoengineering techniques, IMO/FAO/UNESCO-IOC/UNIDO/WMO/IAEA/UN/UN Environment/ UNDP/ISA Joint Group of Experts on the Scientific Aspects of Marine Environmental Protection Rep. Stud. GESAMP No. 98, GESAMP, 2019.

Canadell, J., Monteiro, P., Costa, M., Cotrim da Cunha, L., Cox, P., Eliseev, A., Henson, S., Ishii, M., Jaccard, S., Koven, C., Lohila, A., Patra, P., Piao, S., Rogelj, J., Syampungani, S., Zaehle, S., and Zickfeld, K.: Global Carbon and other Biogeochemical Cycles and Feedbacks, in: Climate Change 2021: The Physical Science Basis. Contribution of Working Group I to the Sixth Assessment Report of the Intergovernmental Panel on Climate Change, edited by Masson-Delmotte, V., Zhai, P., Pirani, A., Connors, S., Péan, C., Berger, S., Caud, N., Chen, Y., Goldfarb, L., Gomis, M., Huang, M., Leitzell, K., Lonnoy, E., Matthews, J., Maycock, T., Waterfield, T., Yelekçi, O., Yu, R., and Zhou, B., pp. 673–816, Cambridge University Press, https://doi.org/10.1017/9781009157896.007, 2021.

Doney, S. C., Wolfe, W. H., McKee, D. C., and Fuhrman, J. G.: The Science, Engineering, and Validation of Marine Carbon Dioxide Removal and Storage, Annual Review of Marine Science, https://doi.org/10.1146/annurev-marine-040523-014702, 2024.

Dunne, J. P., John, J. G., Adcroft, A. J., Griffies, S. M., Hallberg, R. W., Shevliakova, E., Stouffer, R. J., Cooke, W., Dunne, K. A., Harrison, M. J., Krasting, J. P., Malyshev, S. L., Milly, P. C. D., Phillipps, P. J., Sentman, L. T., Samuels, B. L., Spelman, M. J., Winton, M., Wittenberg, A. T., and Zadeh, N.: GFDL's ESM2 Global Coupled Climate–Carbon Earth System Models. Part I: Physical Formulation and Baseline Simulation Characteristics, Journal of Climate, 25, 6646–6665, https://doi.org/10.1175/JCLI-D-11-00560.1, number: 19, 2012.

Dunne, J. P., John, J. G., Shevliakova, E., Stouffer, R. J., Krasting, J. P., Malyshev, S. L., Milly, P. C. D., Sentman, L. T., Adcroft, A. J., Cooke, W., Dunne, K. A., Griffies, S. M., Hallberg, R. W., Harrison, M. J., Levy, H., Wittenberg, A. T., Phillips, P. J., and Zadeh, N.: GFDL's ESM2 Global Coupled Climate–Carbon Earth System Models. Part II: Carbon System Formulation and Baseline Simulation Characteristics*, Journal of Climate, 26, 2247–2267, https://doi.org/10.1175/JCLI-D-12-00150.1, number: 7, 2013.

Fakhraee, M., Li, Z., Planavsky, N. J., and Reinhard, C. T.: A biogeochemical model of mineral-based ocean alkalinity enhancement: impacts on the biological pump and ocean carbon uptake, Environmental Research Letters, 18, 044 047, https://doi.org/10.1088/1748-9326/acc9d4, number: 4, 2023.

Feng, E. Y., Koeve, W., Keller, D. P., and Oschlies, A.: Model-Based Assessment of the CO2 Sequestration Potential of Coastal Ocean Alkalinization, Earth's Future, 5, 1252–1266, https://doi.org/10.1002/2017EF000659, _eprint: https://agupubs.onlinelibrary.wiley.com/doi/pdf/10.1002/2017EF000659, 2017.

Foteinis, S., Campbell, J. S., and Renforth, P.: Life Cycle Assessment of Coastal Enhanced Weathering for Carbon Dioxide Removal from Air, Environmental Science & Technology, 57, 6169–6178, https://doi.org/10.1021/acs.est.2c08633, number: 15, 2023.

https://doi.org/10.5194/egusphere-2025-5917
Preprint. Discussion started: 8 December 2025

Friedlingstein, P., O'Sullivan, M., Jones, M. W., Andrew, R. M., Hauck, J., Olsen, A., Peters, G. P., Peters, W., Pongratz, J., Sitch, S., Le Quéré, C., Canadell, J. G., Ciais, P., Jackson, R. B., Alin, S., Aragão, L. E. O. C., Arneth, A., Arora, V., Bates, N. R., Becker, M., Benoit-Cattin, A., Bittig, H. C., Bopp, L., Bultan, S., Chandra, N., Chevallier, F., Chini, L. P., Evans, W., Florentie, L., Forster, P. M., Gasser, T., Gehlen, M., Gilfillan, D., Gkritzalis, T., Gregor, L., Gruber, N., Harris, I., Hartung, K., Haverd, V., Houghton, R. A., Ilyina, T., Jain, A. K., Joetzjer, E., Kadono, K., Kato, E., Kitidis, V., Korsbakken, J. I., Landschützer, P., Lefèvre, N., Lenton, A., Lienert, S., Liu, Z., Lombardozzi, D., Marland, G., Metzl, N., Munro, D. R., Nabel, J. E. M. S., Nakaoka, S.-I., Niwa, Y., O'Brien, K., Ono, T., Palmer, P. I., Pierrot, D., Poulter, B., Resplandy, L., Robertson, E., Rödenbeck, C., Schwinger, J., Séférian, R., Skjelvan, I., Smith, A. J. P., Sutton, A. J., Tanhua, T., Tans, P. P., Tian, H., Tilbrook, B., Van Der Werf, G., Vuichard, N., Walker, A. P., Wanninkhof, R., Watson, A. J., Willis, D., Wiltshire, A. J., Yuan, W., Yue, X., and Zaehle, S.: Global Carbon Budget 2020, Earth System Science Data, 12, 3269–3340, https://doi.org/10.5194/essd-12-3269-2020, number: 4, 2020.

Fuhr, M., Geilert, S., Schmidt, M., Liebetrau, V., Vogt, C., Ledwig, B., and Wallmann, K.: Kinetics of Olivine Weathering in Seawater: An Experimental Study, Frontiers in Climate, 4, https://doi.org/10.3389/fclim.2022.831587, publisher: Frontiers, 2022.

Griffies, S.: Elements of MOM4p1, GFDL Ocean Group Tech. Rep. 6, 6, 2009.

Hangx, S. J. T. and Spiers, C. J.: Coastal spreading of olivine to control atmospheric CO2 concentrations: A critical analysis of viability, International Journal of Greenhouse Gas Control, 3, 757–767, https://doi.org/10.1016/j.ijggc.2009.07.001, 2009.

Keller, D. P., Feng, E. Y., and Oschlies, A.: Potential climate engineering effectiveness and side effects during a high carbon dioxide-emission scenario, Nature Communications, 5, 3304, https://doi.org/10.1038/ncomms4304, number: 1, 2014.

Keller, D. P., Lenton, A., Scott, V., Vaughan, N. E., Bauer, N., Ji, D., Jones, C. D., Kravitz, B., Muri, H., and Zickfeld, K.: The Carbon Dioxide Removal Model Intercomparison Project (CDRMIP): rationale and experimental protocol for CMIP6, Geoscientific Model Development, 11, 1133–1160, https://doi.org/10.5194/gmd-11-1133-2018, number: 3, 2018.

Köhler, P., Hartmann, J., and Wolf-Gladrow, D. A.: Geoengineering potential of artificially enhanced silicate weathering of olivine, Proceedings of the National Academy of Sciences, 107, 20 228–20 233, https://doi.org/10.1073/pnas.1000545107, publisher: Proceedings of the National Academy of Sciences, 2010.

Köhler, P., Abrams, J. F., Völker, C., Hauck, J., and Wolf-Gladrow, D. A.: Geoengineering impact of open ocean dissolution of olivine on atmospheric CO_2 , surface ocean pH and marine biology, Environmental Research Letters, 8, 014 009, https://doi.org/10.1088/1748-9326/8/1/014009, number: 1, 2013.

Lacroix, F., Burger, F. A., Silvy, Y., Schleussner, C., and Frölicher, T. L.: Persistently Elevated High-Latitude Ocean Temperatures and Global Sea Level Following Temporary Temperature Overshoots, Earth's Future, 12, e2024EF004 862, https://doi.org/10.1029/2024EF004862, number: 10, 2024.

Montserrat, F., Renforth, P., Hartmann, J., Leermakers, M., Knops, P., and Meysman, F. J. R.: Olivine Dissolution in Seawater: Implications for CO_2 Sequestration through Enhanced Weathering in Coastal Environments, Environmental Science & Technology, 51, 3960–3972, https://doi.org/10.1021/acs.est.6b05942, number: 7, 2017.

Nagwekar, T., Nissen, C., and Hauck, J.: Ocean Alkalinity Enhancement in Deep Water Formation Regions Under Low and High Emission Pathways, Earth's Future, 12, e2023EF004 213, https://doi.org/10.1029/2023EF004213, number: 10, 2024.

Najjar, R. and Orr, J.: Design of OCMIP-2 simulations of chlorofluorocarbons, the solubility pump and common biogeochemistry, internal OCMIP report, LSCE/CEA Saclay, Gif-sur-Yvette, France, ocmip5.ipsl.jussieu.fr/OCMIP/phase2/simulations/design.ps, 1998.

National Academies of Sciences, Engineering, and Medicine: A Research Strategy for Ocean-based Carbon Dioxide Removal and Sequestration, National Academies Press, Washington, D.C., https://doi.org/10.17226/26278, pages: 26278, 2022.

https://doi.org/10.5194/egusphere-2025-5917
Preprint. Discussion started: 8 December 2025

Oelkers, E. H., Declercq, J., Saldi, G. D., Gislason, S. R., and Schott, J.: Olivine dissolution rates: A critical review, Chemical Geology, 500, 1–19, https://doi.org/10.1016/j.chemgeo.2018.10.008, 2018.

Pokrovsky, O. S. and Schott, J.: Experimental study of brucite dissolution and precipitation in aqueous solutions: surface speciation and chemical affinity control, Geochimica et Cosmochimica Acta, 68, 31–45, https://doi.org/10.1016/S0016-7037(03)00238-2, 2004.

Renforth, P.: The potential of enhanced weathering in the UK, International Journal of Greenhouse Gas Control, 10, 229–243, https://doi.org/10.1016/j.ijggc.2012.06.011, 2012.

Renforth, P. and Kruger, T.: Coupling Mineral Carbonation and Ocean Liming, Energy & Fuels, 27, 4199–4207, https://doi.org/10.1021/ef302030w, publisher: American Chemical Society, 2013.

Rimstidt, J. D., Brantley, S. L., and Olsen, A. A.: Systematic review of forsterite dissolution rate data, Geochimica et Cosmochimica Acta, 99, 159–178, https://doi.org/10.1016/j.gca.2012.09.019, 2012.

Schwinger, J., Bourgeois, T., and Rickels, W.: On the emission-path dependency of the efficiency of ocean alkalinity enhancement, Environmental Research Letters, 19, 074 067, https://doi.org/10.1088/1748-9326/ad5a27, number: 7, 2024.

Silvy, Y., Frölicher, T. L., Terhaar, J., Joos, F., Burger, F. A., Lacroix, F., Allen, M., Bernardello, R., Bopp, L., Brovkin, V., Buzan, J. R., Cadule, P., Dix, M., Dunne, J., Friedlingstein, P., Georgievski, G., Hajima, T., Jenkins, S., Kawamiya, M., Kiang, N. Y., Lapin, V., Lee, D., Lerner, P., Mengis, N., Monteiro, E. A., Paynter, D., Peters, G. P., Romanou, A., Schwinger, J., Sparrow, S., Stofferahn, E., Tjiputra, J., Tourigny, E., and Ziehn, T.: AERA-MIP: emission pathways, remaining budgets, and carbon cycle dynamics compatible with 1.5 and 2 °C global warming stabilization, Earth System Dynamics, 15, 1591–1628, https://doi.org/10.5194/esd-15-1591-2024, number: 6, 2024.

Terhaar, J., Frölicher, T. L., Aschwanden, M. T., Friedlingstein, P., and Joos, F.: Adaptive emission reduction approach to reach any global warming target, Nature Climate Change, 12, 1136–1142, https://doi.org/10.1038/s41558-022-01537-9, publisher: Nature Publishing Group, 2022.

The Engineering ToolBox: Seawater - Properties, https://www.engineeringtoolbox.com/sea-water-properties-d_840.html, 2005.

Tyka, M. D.: Efficiency metrics for ocean alkalinity enhancements under responsive and prescribed atmospheric pCO_2 conditions, Biogeosciences, 22, 341–353, https://doi.org/10.5194/bg-22-341-2025, number: 1 Publisher: Copernicus GmbH, 2025.

Van Vuuren, D. P., Stehfest, E., Den Elzen, M. G. J., Kram, T., Van Vliet, J., Deetman, S., Isaac, M., Klein Goldewijk, K., Hof, A., Mendoza Beltran, A., Oostenrijk, R., and Van Ruijven, B.: RCP2.6: exploring the possibility to keep global mean temperature increase below 2°C, Climatic Change, 109, 95–116, https://doi.org/10.1007/s10584-011-0152-3, publisher: Springer Science and Business Media LLC, 2011.

Wang, F. and Giammar, D. E.: Forsterite Dissolution in Saline Water at Elevated Temperature and High CO2 Pressure, Environmental Science & Technology, 47, 168–173, https://doi.org/10.1021/es301231n, publisher: American Chemical Society, 2013.

Wanninkhof, R.: Relationship between wind speed and gas exchange over the ocean, Journal of Geophysical Research: Oceans, 97, 7373–7382, https://doi.org/10.1029/92JC00188, _eprint: https://agupubs.onlinelibrary.wiley.com/doi/pdf/10.1029/92JC00188, 1992.

Yang, A. J. K. and Timmermans, M.-L.: Assessing the effective settling of mineral particles in the ocean with application to ocean-based carbon-dioxide removal, Environmental Research Letters, 19, 024 035, https://doi.org/10.1088/1748-9326/ad2236, publisher: IOP Publishing, 2024.

Yang, A. J. K., Timmermans, M.-L., Olsthoorn, J., and Kaminski, A. K.: Influence of stratified shear instabilities on particle sedimentation in three-dimensional simulations with application to marine carbon dioxide removal, Physical Review Fluids, 10, 014 501, https://doi.org/10.1103/PhysRevFluids.10.014501, publisher: American Physical Society, 2025.

https://doi.org/10.5194/egusphere-2025-5917
Preprint. Discussion started: 8 December 2025

Zhou, M., Tyka, M. D., Ho, D. T., Yankovsky, E., Bachman, S., Nicholas, T., Karspeck, A. R., and Long, M. C.: Mapping the global variation in the efficiency of ocean alkalinity enhancement for carbon dioxide removal, Nature Climate Change, 15, 59–65, https://doi.org/10.1038/s41558-024-02179-9, number: 1, 2025.